J Appl Electrochem (2010) 40:1767–1777
DOI 10.1007/s10800-010-0135-5

ORIGINAL PAPER

Single-step polyol synthesis of alloy Pt_7Sn_3 versus bi-phase Pt/SnO_x nano-catalysts of controlled size for ethanol electro-oxidation

Elena A. Baranova · Tariq Amir · Patrick H. J. Mercier · Bussaraporn Patarachao · Dashan Wang · Yvon Le Page

Received: 31 December 2009 / Accepted: 7 April 2010 / Published online: 22 April 2010

Abstract Disordered alloy and bi-phase PtSn nanoparticles of nominal Pt:Sn ratio of 70:30 atomic % with controlled size and narrow size distribution were synthesized using a single-step polyol method. By adjusting the solution pH it was possible to obtain Pt_7Sn_3 nanoparticles of various sizes from 2.8 to 6.5 nm. We found that the presence of NaOH in the synthesis solution not only influenced the nanoparticle size, but as it was revealed by XRD, it apparently also dictated the degree of Pt and Sn alloying. Three catalysts prepared at lower NaOH concentrations ($C_{NaOH} < 0.15$ M) showed disordered alloy structure of the nominal composition, while the other three catalysts synthesized at higher NaOH concentrations ($C_{NaOH} > 0.15$ M) consisted of bi-phase nanoparticles comprising a crystalline phase close to that of pure Pt together with an amorphous Sn phase. These observations are plausibly due to the phase separation and formation of monometallic Pt and amorphous SnO_x phases. A proposed reaction mechanism of Pt_7Sn_3 nanoparticle formation is presented to explain these observations along with the catalytic activities measured for the six synthesized carbon-supported Pt_7Sn_3 catalysts. The highest catalytic activity towards ethanol electro-oxidation was found for the carbon-supported bi-phase catalyst that formed the largest Pt (6.5 nm) nanoparticles and SnO_x phase. The second best catalyst was a disordered alloy Pt_7Sn_3 catalyst with the second largest nanoparticle size (5 nm), while catalysts of smaller size (4.5–4.6 nm) but different structure (disordered alloy vs. bi-phase) showed similar catalytic performance inferior to that of the 5 nm disordered alloy Pt_7Sn_3 catalyst. This work demonstrated the importance of producing bi-metallic PtSn catalysts with large Pt surfaces in order to efficiently electro-oxidize ethanol.

Keywords PtSn catalysts · Ethanol electro-oxidation · Nanoparticles · Polyol synthesis · Disordered alloy

E. A. Baranova (✉) · T. Amir
Department of Chemical and Biological Engineering, University of Ottawa, 161 Louis-Pasteur, Ottawa, ON K1N 6N5, Canada
e-mail: elena.baranova@uottawa.ca

P. H. J. Mercier · B. Patarachao · D. Wang · Y. Le Page
Institute for Chemical Process and Environmental Technology, National Research Council Canada, 1200 Montreal Rd, Ottawa, ON K1A 0R6, Canada

1 Introduction

Direct ethanol fuel cells (DEFCs) are a type of fuel cells developed for portable electronic devices. Ethanol is considered to be an attractive fuel for micro fuel cells due to its non-toxicity and high power density [1]. In addition it can be obtained in great quantity from biomass through a fermentation process of renewable resources such as sugarcane, wheat, corn or straw. Major drawback for implementation of DEFCs is a lack of electro-catalysts which can efficiently break C–C bond and be highly tolerant to poisonous intermediates, e.g., carbon monoxide. Conventional platinum-based catalysts have difficulties to efficiently oxidize ethanol and are easily passivated by the strongly bonded CO_{ads} intermediates [1–3]. One of the ways to improve Pt electrocatalytic performance for ethanol electro-oxidation is a design of bi-metallic nano-structured particles with modified electronic and structural properties. Several studies report ethanol electro-oxidation (EOR) on Pt_xM_{1-x} systems, where M is Sn [2, 4–17], Ru [17–19], Ir [20]. Among investigated bi-metallic systems, Pt_xSn_{1-x} catalysts were found to be most active for EOR [3, 17]. Synthesis procedure has a huge influence on the composition, structure and particle size of PtSn materials, and also has an effect on their

electro-catalytic activity and stability [10–17]. Modified polyol method is suitable to prepare PtSn carbon supported electro-catalysts for EOR, as was demonstrated by Jiang et al. [4, 7, 11] and Zhou et al. [6]. These authors prepared PtSn alloy [4] and bi-phase Pt/SnO_x nanoparticles with different atomic ratios of Pt:Sn = 5:5, 6:4, 7:3, 8:2 [7] by using co-reduction or successive reduction, respectively, of precursor salts in ethylene glycol. They found that $Pt_7(SnOx)_3$ electro-catalysts of 2 nm size consisting of two phases, Pt + SnO_x, was the most active for ethanol electro-oxidation. This was attributed to a good compromise between tin oxide content needed for OH formation and the available active Pt ensembles required for ethanol dehydrogenation and C–C bond splitting. A single DEFC performance test also further showed that $Pt_7(SnO_x)_3/C$ operating at 90 °C had superior activity compared to the other Pt:Sn ratios [7]. Recently Zhu et al. [12] investigated the effect that the alloying degree of Pt_3Sn/C catalyst has on their catalytic activity for EOR. They proposed that PtSn/C catalyst with low alloying degree could enhance the yield of acetic acid via bi-functional mechanism and PtSn/C catalyst with high alloying degree promoted the entire activity for EOR due to an electronic effect.

Despite the large amount of studies devoted to EOR on Pt_xSn_{1-x} electro-catalysts prepared by various chemical and physical methods, no agreement exists in the preferred structure: alloy versus bi-phase, as well as in the optimal composition and particle size of Pt_xSn_{1-x} electro-catalysts for EOR.

In the present work we synthesized carbon-supported Pt_xSn_{1-x} nanoparticles of nominal Pt:Sn ratio of 70:30 atomic % with controlled size and narrow size distribution using a modified polyol method. For the first time, a single-step modified polyol method was used to control (via the synthesis NaOH concentration) both the structure—alloy Pt_7Sn_3 versus bi-phase Pt/SnO_x—and size of resulting Pt_7Sn_3 nano-catalysts. The present work is organized as follows: first, transmission electron microscopy (TEM), X-ray diffraction (XRD) and X-ray photoelectron spectroscopy (XPS) characterization results for the synthesized materials are presented and discussed. This is followed by discussion of a proposed reaction mechanism for the Pt_7Sn_3 nano-catalysts formation and then a comparison of their electro-catalytic activity for ethanol electro-oxidation reaction.

2 Experimental section

2.1 Catalyst synthesis

2.1.1 Unsupported nanoparticles

Tin(II) chloride anhydrous (ACROS Organics, 98% Anhydrous) and Platinum(IV) chloride (Alfa Aesar, 99.9% metal basis, Pt (57.75%)) were used as precursor salts. Synthesis of Pt_7Sn_3 nanoparticles was carried out in ethylene glycol solution (anhydrous 99.8% Sigma-Aldrich). First, precursor salts were dissolved in ethylene glycol containing appropriate amount of NaOH (EM Science, ACS grade). The solution was stirred for 1 h at room temperature and then refluxed at 190 °C for 2 h. Dark brown solutions containing Pt_7Sn_3 colloids were formed in this manner. Table 1 summarizes the synthesis conditions for Pt_7Sn_3 nanoparticles prepared in the present work.

Table 1 Synthesis conditions of Pt_7Sn_3 nanoparticles in 50 mL of ethylene glycol

Catalyst no.	$mSnCl_2$ (g)	$mPtCl_4$ (g)	C_{NaOH} (M)	m_{Carbon} (g)	Final pH
1	0.0223	0.0932	0.08	0.2174	8
2	0.0223	0.0923	0.10	0.2157	7
3	0.0225	0.0915	0.12	0.2146	9
4	0.0229	0.0927	0.15	0.2180	10
5	0.0230	0.0932	0.20	0.2190	9
6	0.0230	0.0935	0.30	0.2200	9

2.1.2 Carbon supported Pt_7Sn_3 nanoparticles

Appropriate aliquots of the colloidal solutions were mixed with carbon black (Vulcan XC-72R, Cabot, corporation) in a large beaker for up to 24 h, resulting in the deposition of the colloids on the carbon substrates. Pt_7Sn_3 loadings of 20 weight (wt) % on carbon were prepared in this manner. The carbon supported Pt_7Sn_3 catalysts were filtered and extensively washed with nanopure water (18 MΩ cm) and then dried in air at 80 °C for 3 h.

2.2 Physicochemical characterization of Pt_7Sn_3 nanoparticles

2.2.1 TEM and EDS

Transmission electron microscopy (TEM) analysis of unsupported Pt_7Sn_3 and carbon-supported Pt_7Sn_3/C catalyst were carried out using a JEOL JEM 2100F FETEM microscope operating at 200 kV. The samples were prepared for TEM analysis by sonicating the Pt_7Sn_3 unsupported colloids with ethylene glycol for 10 min while carbon-supported nanoparticles were suspended in ethanol. A drop of as-prepared colloid or carbon-supported catalysts were applied directly onto clean copper grids and dried in the oven at 80 °C for 2 h. The size distribution and the mean particle size of each sample were obtained by measuring ~300 particles from bright field micrographs.

Bulk elemental composition of the resulting Pt_7Sn_3 nanoparticles deposited on carbon support was studied

using energy dispersive X-ray analysis (EDS). The EDS analysis was performed using a JEOL JSM-7500F field emission scanning electron microscope equipped with an energy dispersive X-ray spectrometer (Oxford Instrument). The spectra were acquired at an acceleration voltage of 20 kV and magnification of 500. EDS analysis supported that atomic composition of the samples was close to the nominal 7:3 at. ratio of Pt to Sn.

2.2.2 XRD

The X-ray diffraction powder patterns were collected using a Bruker AXS D8 Advance system θ–θ powder diffractometer, equipped with a Cu tube and a Vantec position-sensitive detector with radial Soller slits to reduce the background at low angles. The diffractograms were collected between 30° and 100° 2θ with a step of 0.0142° 2θ. The Pt_7Sn_3/C 20 wt% catalyst samples were deposited in a flat-surfaced, semi-infinite filled trough machined into a low-background single-crystal silicon wafer holder and then gently pressed flat using a glass slide. The average crystallite sizes for the Pt_7Sn_3/C catalysts were evaluated using the full width at half maximum (FWHM) and full width at three-quarter maximum (3/4). The width of the Pt (220) peak was used to calculate the average crystallite size according to the Debye's formula based on the spherical Pt, $Pt_{3/4}Sn_{1/4}$ and $Pt_{2/3}Sn_{1/3}$ cluster models [21, 22]. Scattering profiles for Pt nanoparticles were calculated on clusters containing between 100 and 35,000 atoms derived assuming a cubic cell parameter $a = 3.9231$ Å. For $Pt_{3/4}Sn_{1/4}$ and $Pt_{2/3}Sn_{1/3}$ compositions, cell parameter values of respectively 3.9694 and 3.9848 Å were assumed based on a linear extrapolation from Pt to the value of $a = 3.9416$ Å measured for bulk Pt_9Sn alloy [23]. For these two compositions, random site-occupation cluster models were obtained by duplicating four times ($Pt_{3/4}Sn_{1/4}$) or three times ($Pt_{2/3}Sn_{1/3}$) the set of atom coordinates generated for a starting spherical Pt cluster of given diameter size, then replacing the correct proportion of Pt atoms by Sn atoms, and finally multiplying by 1/16 ($Pt_{3/4}Sn_{1/4}$) or 1/9 ($Pt_{2/3}Sn_{1/3}$) the resulting diffraction intensities calculated using Debye formula. Both the cluster generation and profile calculations were performed with *Materials Toolkit* [24] and using Debye formula for scattering by randomly oriented molecules, as described in details in [22].

2.2.3 XPS

Pt_7Sn_3 catalysts were analyzed by X-ray photoelectron spectroscopy equipped with a KRATOS Axis Ultra DLD that has a Hybrid lens mode. The XPS analysis was conducted at 140 W and at pass energy of 20 eV. The peak positions were corrected for sample charging by setting the C 1s binding energy at 284.4 eV. The carbon supported Pt_7Sn_3 catalysts were deposited on a sample holder and vacuumed to get rid of excess impurities in the sample. For comparison of binding energies, carbon-supported Pt catalysts of 3.5 nm size and pure Pt foil were run at the same conditions.

2.3 Electrochemistry

All electrochemical measurements were conducted using Parstat 2273 Advanced Electrochemical System (Princeton Applied Research) in conjunction with Electrochemical Power Suite version 2.58 (Advanced Measurement Technology, Inc.) for Windows software program.

2.3.1 Electrochemical cell and electrolyte solutions

Experiments were carried out in a Pyrex three-compartment electrochemical cell. During the experiments, H_2 gas (99.997% Linde Canada Limited) was bubbled through the Pt/Pt-black reference electrode compartment. High-purity Ar gas (99.998% Linde Canada Limited) was passed through the working electrode compartment. The large surface area gauze Pt counter electrode was contained in a separate compartment. All potentials were measured with respect to a reversible hydrogen electrode (RHE) immersed in the supporting electrolyte solution (0.5 M H_2SO_4) in a separate compartment provided with a Luggin capillary. The sulfuric acid (Fisher-Scientific, 98% ACS grade), ethanol (Commercial Alcohols Inc., 100% ACS grade) and nanopure water (18 MΩ cm) were used to prepare solutions.

2.3.2 Working electrode

A glassy carbon disc electrode (GC DE) (0.196 cm^2 geometrical surface area, Pine Research Instrumentation Company) was used as a working electrode. The working electrode was a carbon-supported Pt_7Sn_3 composite cast on a carbon disk electrode. The catalyst powders were formed into electrodes by sonicating 13 mg of the carbon-supported catalyst powders in 1 mL of H_2O and 300 μL of Nafion solution for 15 min, forming a catalyst ink. Subsequently 2.5 μL of catalyst ink was applied to a glassy carbon disc. The catalyst layer was then dried in air at 80 °C for 30 min. All electrochemical experiments were carried out at room temperature.

2.3.3 Cyclic voltammetry and chronoamperometry

Cyclic voltammograms (CVs) were carried out at 10 mV s^{-1} in 0.5 M H_2SO_4 starting from the open circuit potential for 10 cycles between the potential limits of 0.1–1.1 V. The ethanol electro-oxidation was performed at

10 mV s^{-1} in a nitrogen purged solution of 1.0 M C_2H_5OH + 0.5 M H_2SO_4 between 0.1 and 1.0 V starting from open circuit potential for 25 cycles. Here we present the forward scan of the 25th cycle. For chronoamperometric (CA) measurements, the potential was first held at 0.1 V for 300 s, then stepped to 0.5 V for 1 h. Nitrogen gas was bubbled through the electrolyte solution before and during the 1 h experiment.

3 Results and discussion

3.1 TEM of unsupported and carbon-supported Pt_7Sn_3 nanoparticles

Typical TEM micrographs and corresponding histograms of particle size distribution for the as-prepared colloidal and carbon-supported Pt_7Sn_3 catalysts synthesized using sodium hydroxide concentration of 0.15 M are shown in Fig. 1. It can be seen that the resulting Pt_7Sn_3 colloidal nanoparticles (Fig. 1a) are spherical in shape and show narrow particle size distribution. We found some degree of particle agglomeration that likely took place over time after synthesis. Nevertheless, the identity of individual particles was recognizable even for agglomerated particles. Pt_7Sn_3 particles with a mean size diameter of 2.5–8 nm were prepared depending on the synthesis solution pH. The smallest Pt_7Sn_3 nanoparticles, of 2.5 ± 1 nm in diameter, were synthesized using NaOH concentration of 0.15 M. After the same nanoparticles were deposited on carbon (Fig. 1b), we observed a slight increase in the particle size and presence of agglomerates. This could be related to the procedure of nanoparticle deposition on carbon substrate, which involved stirring and may have lead to particle agglomeration. A summary of the average particle sizes obtained by TEM for colloidal and carbon-supported Pt_7Sn_3 nanoparticles is shown in Table 2. Overall, the TEM observations showed that the platinum-tin nanoparticles prepared in this work were of narrow size distribution, although the size distribution increased somewhat as larger nanoparticles were made.

3.2 XRD of carbon-supported Pt_7Sn_3 catalysts

Experimental XRD patterns obtained for the carbon-supported Pt_7Sn_3 catalysts are shown in Fig. 2. Figure 2a, b show XRD patterns for catalysts prepared at C_{NaOH} between 0.08 and 0.12 M and Fig. 2c, d for larger NaOH concentrations of 0.15–0.3 M. As can be seen from the figure, all catalysts synthesized in the present work show

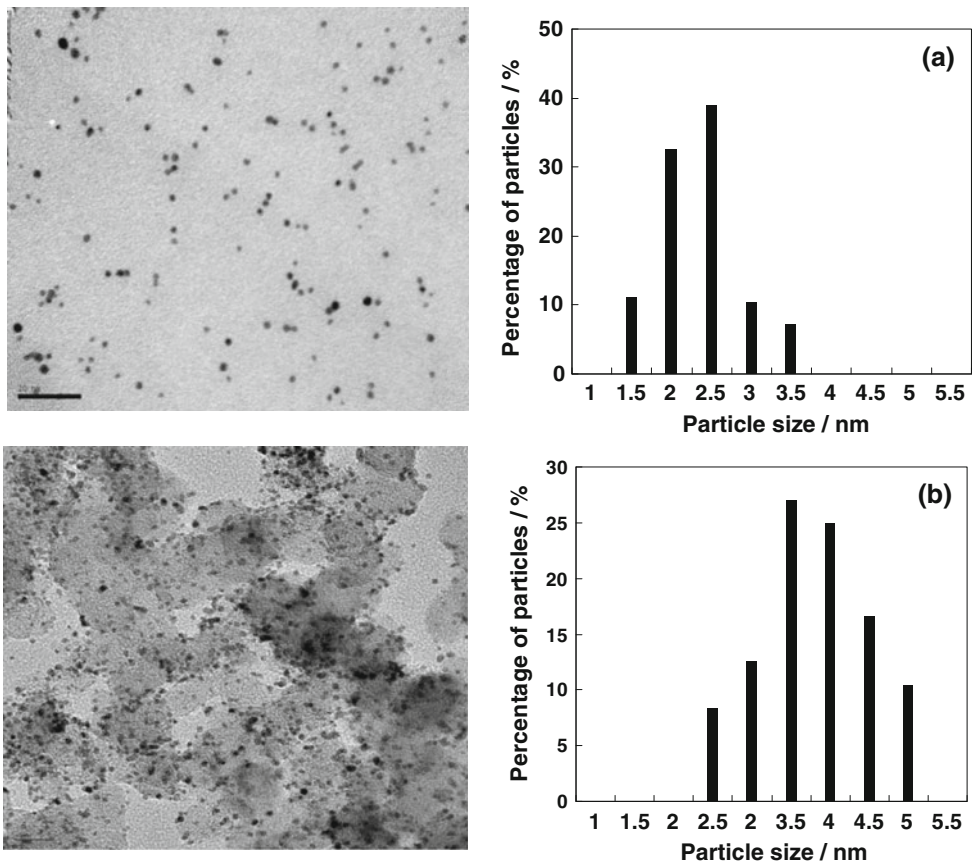

Fig. 1 TEM images (*left*) and corresponding histograms (*right*) of Pt_7Sn_3 unsupported (**a**) and carbon supported (**b**) catalyst no. 4, synthesized in ethylene glycol using NaOH concentration of 0.15 M. The bar in **a** and **b** indicates 20 nm scale

Table 2 Average particle size obtained from TEM and XRD, $2\theta_{max}$, full-width at half maximum (FWHM) and full width at ¾ maximum (FW3/4M) of (220) *fcc* peak, electrochemical active surface area ($EASA_{H_2}$) and current density at 0.2 V (Fig. 8) of Pt_7Sn_3 catalysts

Catalyst no.	C_{NaOH} (M)	Average particle size (nm) TEM	Average particle size (nm) XRD	$2\theta_{max}$ of (220) (°±0.01°)	FWHM (°) 2θ	$FW^3/_4M$ (°) 2θ	$EASA_{H_2}$ ($m^2\ g_{Pt}^{-1}$)	i at 0.2 V ($\mu A\ cm^{-2}$)
1	0.08	–	4.2	66.47	2.91	1.83	33.70	10.16
2	0.10	6.0	5.0	66.53	2.56	1.53	7.685	65.42
3	0.12	5.5 (4.5[a])	4.5	66.56	2.69	1.67	13.38	35.80
4	0.15	3.5 (2.5[a])	2.8	67.16	4.07	2.51	76.41	5.790
5	0.20	5.8	4.6	67.37	2.88	1.53	10.5	38.55
6	0.30	8.5	6.5	67.43	1.92	1.18	4.893	155.5

[a] Particle size for unsupported Pt_7Sn_3 nanoparticles

face-centered cubic (*fcc*) structure typical for bulk and nano-structured Pt [22, 25]. Peaks around 40, 46, 68 and 81°2θ correspond to Pt-type *fcc* reflections (111), (200), (220) and (311), respectively. Only the Pt_7Sn_3 catalyst prepared using the lowest sodium hydroxide concentration ($C_{NaOH} = 0.08$ M) was found to have additional peaks at 34° and 52°, which correspond to crystalline-phase SnO_2 (101) and (211) reflections. There was no separate crystalline-phase SnO_2 observed for any other carbon-supported Pt_7Sn_3 samples.

As we pointed out recently [26], carbon Vulcan XC-72 has reflections near 25 and 45°2θ, which correspond respectively to graphite reflections 002 and 101. As these two peaks overlap with the main *fcc* (111) and (200) diffraction peaks, the present analysis of XRD patterns was therefore carried out at the *fcc* (220) peak around 68° 2θ (Fig. 2b, d). This peak does not overlap with any diffraction peaks from carbon Vulcan XC-72. Accordingly, the (220) reflection was thus used to calculate the average crystallite size according to Debye formula for scattering by randomly oriented molecules [21] as we demonstrated in [22] for colloidal Pt and Pt_xRu_{1-x}, as well as in [26] for carbon-supported Pd_xPt_{1-x} catalysts. The average crystallite size was estimated using the full width at half maximum (FWHM) and full width at 3/4 maximum (FW3/4M) of the *fcc* (220) as described in [22]. The 2θ position at maximum intensity ($2\theta_{max}$) for reflection (220) was derived from a third order polynomial fit close to the top of the peak [22]. Table 2 summarizes the average particle sizes of the carbon-supported Pt_7Sn_3 catalysts estimated by XRD, along with $2\theta_{max}$, FWHM and FW3/4M of (220) peak.

It is clear from Fig. 2b and d that the (220) peak is shifted to lower 2θ values compared to the 220 position for bulk *fcc* Pt. The observed shift for the (220) peak can be related to the alloy formation as well as to the small-particle size effect [22, 23]. The latter can be very pronounced for nanoparticles smaller than 5 nm as shown earlier in [22] and also seen in Fig. 3. Figure 3 reports the Cu K_α 2θ positions at maximum intensity calculated for the 220 peak versus the nanoparticle diameter size for clusters of Pt (a), $Pt_{2/3}Sn_{1/3}$ (b) and $Pt_{3/4}Sn_{1/4}$ (c) compositions. These calculated values (filled black circles linked with solid lines) were extracted numerically from the results of simulated powder-diffraction profiles as described in Sect. 2.2.2 on a series of Pt_xSn_{1-x} spherical cluster models. Note that the observed shift in the 2θ position resulting from the small-particle size effect reaches 1.45^o 2θ for particles with diameter of 1.0 nm for all three compositions considered.

Figure 3 also shows experimental $2\theta_{max}$ of (220) peak for Pt_7Sn_3 catalysts prepared in this work (open triangles). By comparing the experimental results with the theoretically calculated curves, it is clear that two distinct sets of observations directly follow for catalysts nos. 1, 2, 3 compared to nos. 4, 5, 6. First, nanoparticles with a disordered alloy structure of the nominal Pt:Sn ratio of 7:3 were formed only for catalysts nos. 1, 2 and 3. These samples correspond to the three smallest NaOH concentrations used for synthesis (Table 1). For catalysts nos. 4, 5 and 6, prepared using higher NaOH concentrations of respectively 0.15, 0.2 and 0.3 M, only partial alloying occurred and nanoparticles with a structure and composition close to that of pure Pt were formed. No evidence of metallic Sn or SnO_2 crystalline phases were found on XRD patterns for these three catalysts, suggesting that the Sn content observed by EDS analysis is present in an amorphous state. We conclude that bi-phase Pt/SnO_x nanocatalysts were synthesized at the higher NaOH concentrations used for samples nos. 4, 5, 6.

In conclusion to this XRD section, we would like to point out that by adjusting solution pH we were able to obtain Pt_7Sn_3 nanoparticles of various sizes from 2.8 to 6.5 nm. We would like to stress that the presence of NaOH in the synthesis solution not only influenced the nanoparticle size, but as it was revealed by XRD, it apparently also dictated the degree of Pt and Sn alloying that occurred. Nanoparticles prepared at the larger NaOH concentrations

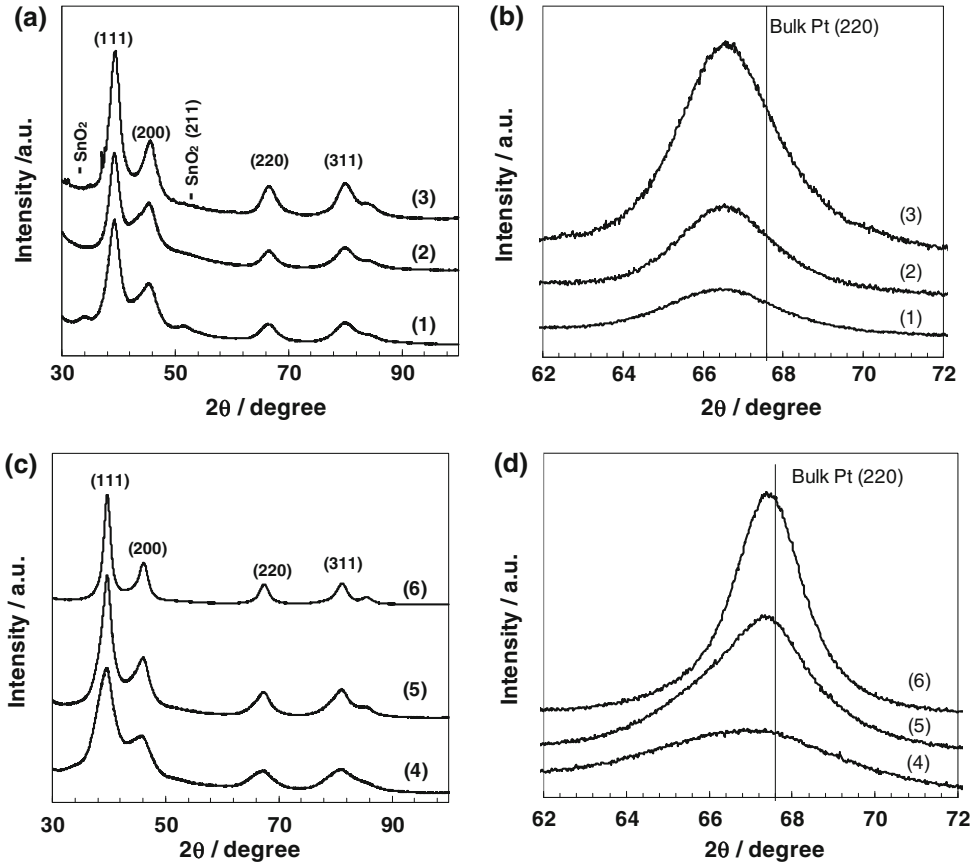

Fig. 2 Slow scan XRD pattern of the carbon supported Pt_7Sn_3 catalysts in the broad range of 2θ **a** + **c** and zoom to fcc (220) peak **b** + **d**. *Numbers in parenthesis* refer to the catalyst nos. identified in Table 2

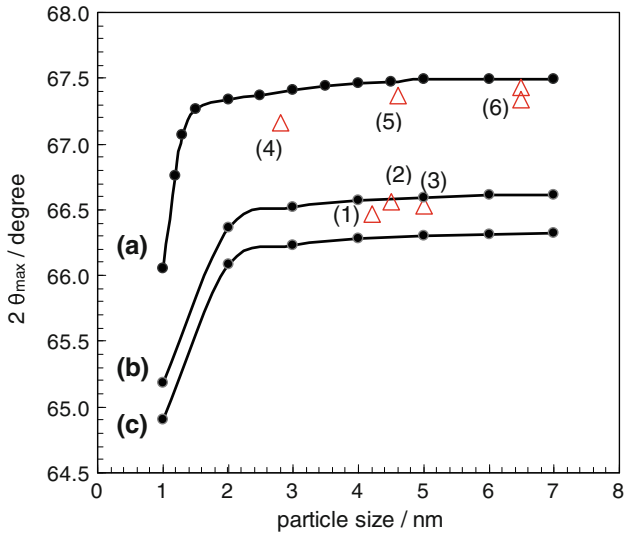

Fig. 3 Cu K_α 2θ angle at maximum peak intensity versus cluster diameter. *Filled circles* linked with solid lines correspond to simulations using Debye formula for: Pt clusters (*a*); $Pt_{2/3}Sn_{1/3}$ clusters (*b*); $Pt_{3/4}Sn_{1/4}$ clusters (*c*); *open triangles* correspond to experimental $2\theta_{max}$ angles of carbon supported Pt_7Sn_3 catalysts. *Numbers in parenthesis* refer to the catalyst nos. identified in Table 2

($C_{NaOH} > 0.15$ M) showed compositions close to that of pure Pt, however XRD did not reveal the presence of any crystalline Sn or SnO_2 phases. This is plausibly due to phase separation and formation of monometallic Pt and amorphous Sn phases. A possible explanation to this observation related to the mechanism of Pt_7Sn_3 nanoparticle formation is presented in Sect. 3.4 below.

3.3 XPS of carbon-supported catalyst

Atomic surface compositions of Pt_7Sn_3 catalysts supported on carbon were determined by X-ray photoelectron spectroscopy. For this purpose, the integrated areas measured under the Pt 4f, C 1s, O 1s, and Sn 3d core level peaks were used. Figure 4 shows the variation of the Pt and Sn surface concentration with respect to the NaOH concentration in the synthesis solution. Surface composition appeared close to the nominal 7 to 3 atomic ratio of Pt to Sn in most cases (catalysts nos. 1, 4, 5 and 6). For catalysts nos. 2 and 3, prepared at respectively C_{NaOH} of 0.1 and 0.12 M, an apparent surface enrichment by Sn is found. The surface energies of Pt and Sn are $\gamma_{Pt} = 2.34$ J cm^{-2} and $\gamma_{Sn} = 0.57$ J cm^{-2}, respectively. It is then reasonable to expect that the surface of alloyed nanoparticles would contain excess of Sn, because this would minimize the energy of the system. The binding energies of Pt and Sn in carbon-supported Pt_7Sn_3 catalysts as obtained from the fitting of higher resolution Pt 4f and Sn 3d core level XPS

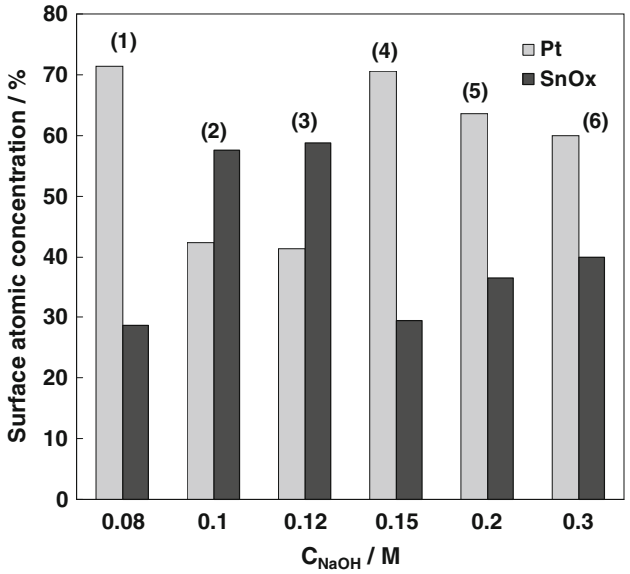

Fig. 4 Variation of the surface atomic concentration of carbon supported Pt_7Sn_3 catalysts with respect to sodium hydroxide concentration. *Numbers in parenthesis* refer to the catalyst nos. identified in Table 2

spectra are given in Tables 3 and 4, respectively. In addition, Table 3 shows binding energies for Pt bulk foil and carbon supported Pt nanoparticles of 3.5 nm size obtained at the same experimental conditions as XPS spectra measured for Pt_7Sn_3 catalysts. The Pt $4f_{7/2}$ core level peaks were fitted using two components. The peak at ~71.3 eV was assigned to Pt (0) and the peak around 72.0 eV to PtO. A shift to lower binding energies was observed for carbon-supported Pt_7Sn_3 nanoparticles compared to the values for Pt nanoparticles. This may come from the electronic interaction between Pt and Sn, since the respective elemental electronegativity values for Sn and Pt are 1.8 and 2.2 [27]. Pt atoms could produce an electron withdrawing effect from Sn atoms changing the polarization of Pt–Sn bonds [28, 29].

The Sn $3d_{5/2}$ core level peaks were deconvoluted using two components. The peak at ~485 eV was assigned to Sn metal and at ~487 eV to tin oxide SnO_x. Binding energies for SnO_2 and SnO are quite similar at 486.4 and 486.6 eV, respectively. Consequently, it was difficult to distinguish between these two species. The binding energies of Sn in all carbon-supported Pt_7Sn_3 catalyst samples are higher than the reference values [30]. This might be due to the electronic effect generated between Pt and Sn metal interaction or the small-particle size effect [31]. XPS was able to confirm that the main part of Sn is in the oxidized state.

3.4 Proposed reaction mechanism of nanoparticle formation during synthesis

In the present work Pt_7Sn_3 nanoparticles of different structure, disordered alloy versus bi-phase Pt/SnO_x, with controlled size were formed by varying the sodium hydroxide concentration in the synthesis solution. Figure 5 shows the average particle size of the synthesized carbon-supported Pt_7Sn_3 nanoparticles, found from XRD analysis, as a function of NaOH concentration. For convenience, we divided this graph into three regions according to

Table 3 Parameters extracted from analysis of Pt $4f_{7/2}$ core level XPS spectra of carbon supported Pt_7Sn_3

Catalyst no.	Average particle size[a] (nm)	C_{NaOH} (M)	Species	Binding energy of Pt $4f_{7/2}$		
				Binding energy (eV)	FWHM (eV)	Atomic conc. (at.%)
1	4.2	0.08	Pt	71.2	0.9	71.4%
			PtO	71.9	1.6	
2	5.0	0.10	Pt	71.2	0.8	42.4%
			PtO	71.9	1.6	
3	4.5	0.12	Pt	71.3	1.0	41.3%
			PtO	72.2	1.6	
4	2.8	0.15	Pt	71.3	0.9	70.5%
			PtO	72.0	1.4	
5	4.6	0.20	Pt	70.9	0.9	63.6%
			PtO	71.95	1.5	
6	6.5	0.30	Pt	71.1	0.8	60.0%
			PtO	71.9	1.5	
Pt/C	3.5	n.a.	Pt	71.5	1.2	n.a.
			PtO	72.3	2.3	
Bulk Pt foil	n.a.	n.a.	Pt	70.9	1.0	n.a.

[a] From XRD analysis

Table 4 Parameters extracted from analysis of Sn $3d_{5/2}$ core level XPS spectra of carbon supported Pt_7Sn_3

Catalyst no.	Average particle size[a] (nm)	C_{NaOH} (M)	Species	Binding energy of Sn $3d_{5/2}$		
				Binding energy (eV)	FWHM (eV)	Atomic conc. (at.%)
1	4.2	0.08	Sn	485.1	1.3	28.6
			SnO_x	487.1	1.4	
2	5.0	0.10	SnO_x	486.9	1.4	57.6
3	4.5	0.12	Sn	485.3	0.9	58.7
			SnO_x	487.3	1.4	
4	2.8	0.15	Sn	484.8	1.0	29.5
			SnO_x	486.7	1.3	
5	4.6	0.20	Sn	485.1	0.8	36.4
			SnO_x	486.6	1.3	
6	6.5	0.30	SnO_x	485.8	1.5	40.0

[a] From XRD analysis

C_{NaOH}. In region 1 ($C_{NaOH} < 0.08$ M), Pt_7Sn_3 nanoparticles could not be formed and large micron-size particles were found in the solution. It is related to the mechanism of nanoparticle stabilization. Prepared in the present study PtSn nanoparticles were stabilized by one of the products of ethylene glycol oxidation, i.e., the glucolate [32, 33]. At low pH it is mostly present in its protonated form, i.e., glycolic acid, which may explain formation of micro-sized particles in the region 1 of Fig. 5. In region 2 (C_{NaOH} ranges from 0.08 to 0.15 M), we observed formation of disordered alloy nanoparticles with average size of 4.2–5 nm. At C_{NaOH} larger than 0.15 M (region 3), bi-phase Pt/SnO_x nanoparticles were formed. It can be seen that both structure and particle size were related to the presence of NaOH, as was also previously demonstrated for mono-metallic Pt and Ru, as well as bi-metallic Pt/Ru nanoparticles [32, 33]. Whereas it was demonstrated in [32] that the size of Pt nanoparticles

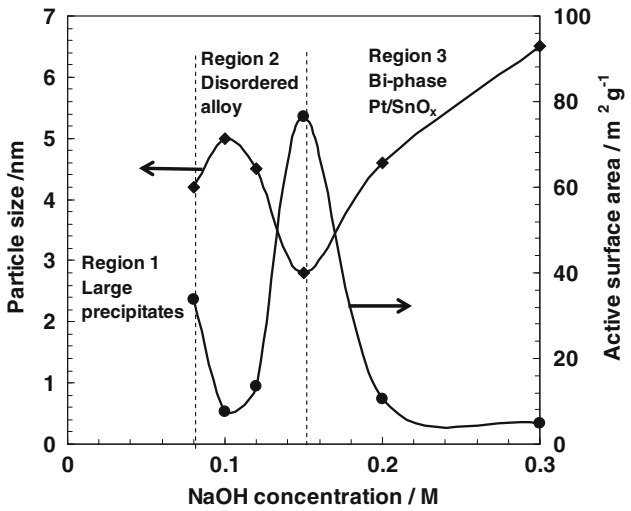

Fig. 5 Effect of NaOH concentration on the average particle size of carbon supported Pt_7Sn_3 nanoparticles and on the calculated active electrochemical surface area (Eq. 3)

increases with decreasing solution pH, this was not the case for the Pt_7Sn_3 nanoparticles prepared in the present work (Fig. 5). In fact, an opposite trend was observed here and this behavior may be explained by the interaction of NaOH with $SnCl_2$ precursor salt resulting in the formation of poorly soluble $Sn(OH)_2$ compound:

$$Sn^{2-} + 2OH^- \rightarrow Sn(OH)_2 + 2Cl^-. \quad (1)$$

Poorly soluble $Sn(OH)_{2(s)}$ plausibly serves as a nucleation site for nanoparticle growth leading to initial formation of Sn core—Pt shell particle. Due to the difference in Pt and Sn atomic sizes, atoms would tend to redistribute in order to minimize energy of the system. This was apparently the case for region 2 where lower NaOH concentrations were used for synthesis and disordered alloy Pt_7Sn_3 nanoparticles were formed (Fig. 5). For alloy Pt_xM_{1-x} nanoparticles where Pt is mixed with a metal M giving rise to a larger cubic cell parameter, it is expected that the minimum energy will correspond to an M-enriched surface. This was indeed observed by XPS where a surface enrichment in Sn is noted for catalysts nos. 2 and 3 (Fig. 4). However, in the presence of excess of sodium hydroxide (region 3, Fig. 5), a poorly soluble $Sn(OH)_2$ is transformed to a soluble compound according to the reaction:

$$Sn(OH)_2 + 2OH^- \rightarrow Sn(OH)_4^{2-} \rightleftarrows SnO_2^{2-} + 2H_2O. \quad (2)$$

Poorly soluble $Sn(OH)_2$ and soluble SnO_2^{2-} compounds may then co-exist in the synthesis solution. Therefore Pt_xSn_{10-x} ($x < 7$) nanoparticles may form starting from $Sn(OH)_2$ nucleation sites, while $SnO_2^{2-}{}_{(aq)}$ is reduced by ethylene glycol and could be re-deposited on the surface of Pt_xSn_{10-x} nanoparticles or form a separate phase. This apparently was indeed observed in the region 3, Figs. 5 and 3 (catalyst nos. 4, 5 and 6). Note that for region 3, the size of synthesized nanoparticles increased as C_{NaOH} was increased.

3.5 Electrochemistry

3.5.1 Cyclic voltammetry in 0.5 M H_2SO_4

Carbon supported Pt_7Sn_3 catalysts synthesized in the present work were first studied in a half molar sulphuric acid in order to evaluate their electrochemical active surface areas (EASA). Figure 6 shows typical cyclic voltammograms of carbon-supported Pt_7Sn_3 catalysts (catalyst nos. 1, 4 and 6) in 0.5 M H_2SO_4. The electrochemical active surface areas were calculated using the hydrogen desorption peak area in the CV curves between 0.1 and 0.3 V versus RHE. The EASA can be calculated from the following equation [34]:

$$\text{EASA}\left(\text{m}^2\,g^{-1}\right) = \frac{Q_H}{0.21 * [\text{Pt}]} \quad (3)$$

where Q_H (mC cm^{-2}) represents the charges exchanged during the desorption of hydrogen on the Pt surface, [Pt] (mg cm^{-2}) is the Pt loading in the electrode, and 0.21 (mC cm^{-2}) is the charge required to oxidize the monolayer of hydrogen on the Pt surface. The calculated EASA values of all Pt_7Sn_3 catalysts are summarized in the Table 2 and Fig. 5. As expected larger particles showed smaller surface area. The largest active surface area was found for Pt_7Sn_3 catalyst no. 4, which had particle size of 2.8 nm and bi-phase Pt/SnO_x structure.

3.5.2 Electro-oxidation of ethanol on carbon-supported Pt_7Sn_3 nanoparticles

Catalytic activities of Pt_7Sn_3 catalysts for ethanol electro-oxidation were characterized using cyclic voltammetry and chronoamperometry. Figure 7 shows a forward scan of the cyclic voltammogram for carbon-supported Pt_7Sn_3 catalysts in 1.0 M C_2H_5OH + 0.5 M H_2SO_4. Current densities are given per calculated EASA (Eq. 3) and Table 2 summarizes current densities obtained at 0.2 V versus RHE. For catalyst nos. 1, 2 and 3 with disordered alloy structures (Fig. 7, thin solid line), the lowest current density was obtained for catalyst no. 1 that had the smallest particle size among these catalysts (nos. 1, 2 and 3), while behaviors of catalysts nos. 2 and 3 were quite similar due to their comparable particle size and structure (although slightly better activity was observed for no. 2 compared to no. 3). Among the set of bi-phase Pt/SnO_x structures (Fig. 7, thick solid line; catalysts nos 4, 5 and 6), the catalyst no. 6, which consisted of large 6.5 nm Pt nanoparticles and an SnO_x phase, had the lowest overpotential (0.1 V vs. RHE) and highest current density for ethanol electro-oxidation. The overpotentials for the catalyst nos. 2, 3 and 5 were 0.2 V, while for nos 1 and 4 were 0.25 V. Obtained overpotentials are comparable to those reported recently by Zhu et al. [12] for binary PtSn catalysts with varied degree of alloying. For bi-phase $PtSnO_2/C$ catalysts, authors

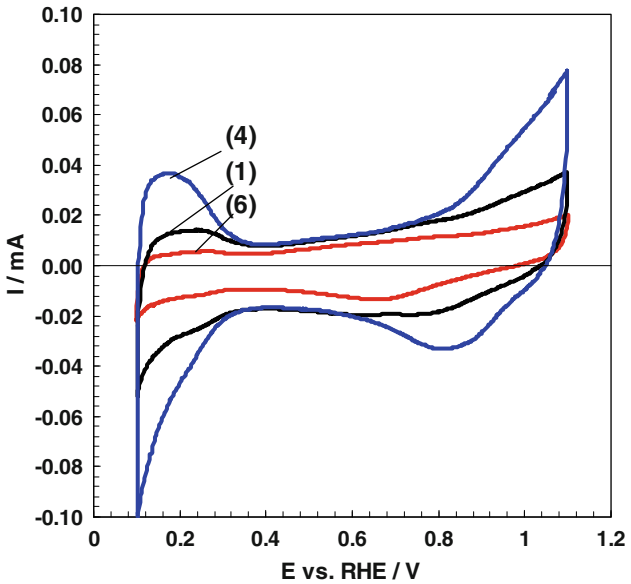

Fig. 6 Cyclic voltammograms of carbon supported Pt_7Sn_3 catalysts in 0.5 M H_2SO_4 with a sweep rate of 10 mV s^{-1}. *Numbers* shown refer to the catalyst nos. identified in Table 2

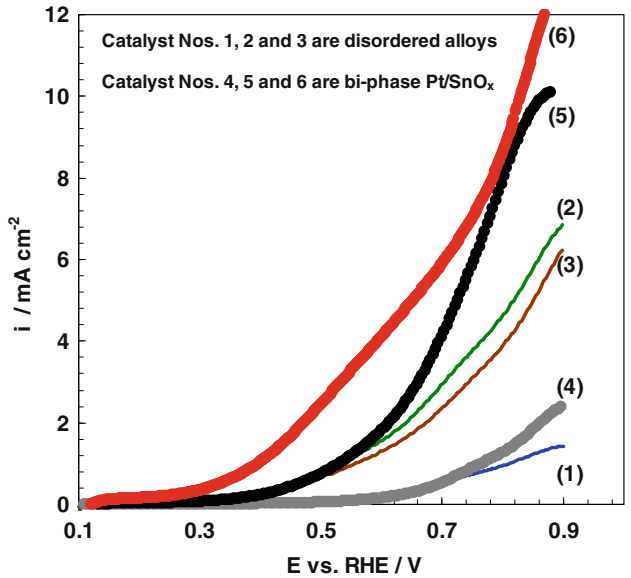

Fig. 7 Cyclic voltammograms (*forward scan*) of carbon supported Pt_7Sn_3 catalysts in 1.0 M C_2H_5OH + 0.5 M H_2SO_4 at a sweep rate of 10 mV s^{-1}. Current densities are given per electrochemical active surface area (EASA). *Numbers* shown refer to the catalyst nos. identified in Table 2

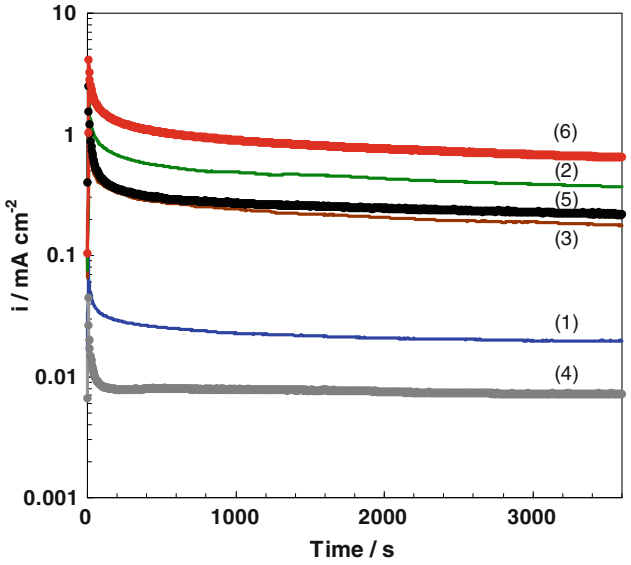

Fig. 8 Chronoamperograms of carbon supported Pt_7Sn_3 catalysts in 1.0 M C_2H_5OH + 0.5 M H_2SO_4 at 0.5 V versus RHE. *Numbers* shown refer to the catalyst nos. identified in Table 2

reported the onset potential of 0.1 V, while for alloyed catalyst it varied from 0.17 to 0.25 V versus RHE, depending on alloying degree.

Chronoamperometric measurements were used to analyze the steady-state performance of the catalysts (Fig. 8). The stability of the Pt_xM_{1-x} catalysts is a big concern for applications in fuel cells [1–3]. There might be possible degradation such as sintering and dissolving of catalysts during operation which could affect the fuel cell performance. Resulting i–t curves are shown in Fig. 8, as thin and thick solid lines for disordered alloy Pt_7Sn_3 and bi-phase Pt/SnO_x catalysts, respectively. These measurements were carried out after recording CVs in ethanol. All curves in Fig. 8 have similar shape with three regions. The first region, which lasts only several minutes, is characterized by a rapid drop of current. In the second region the current decrease is less steep and in the third, the current reaches a steady-state value. The decrease of current in the first and second regions is attributed to a rapid increase of the surface coverage by partially oxidized species that block Pt surfaces, diminishing its ability to electro-oxidize ethanol [7, 8, 11]. Observed catalytic behaviour was similar to CVs and the highest steady-state current density was found for the bi-phase Pt (6.5 nm)/SnO_x catalyst. The steady-state current density decreased in the following sequence: 6.5 nm (bi-phase no. 6) > 5 nm (disordered alloy no. 2) > 4.6 nm (bi-phase no. 5) > 4.5 nm (disordered alloy) > 4.2 nm (disordered alloy no. 1) > 2.8 nm (bi-phase). From this comparison, we can see that structure, i.e., alloy versus bi-phase, played a role in catalyzing ethanol electro-oxidation but that particle size was more important. Promotion of EOR was facilitated on larger Pt (6.5 nm)/SnO_x and Pt_7Sn_3 (5 nm) particles suggesting that larger Pt surfaces are required for ethanol adsorption and further conversion to reaction products. Both the bi-functional mechanism and electronic effect have been proposed to be involved in the ethanol electro-oxidation over Pt_xSn_{1-x} [1–3, 35]. Adsorption and decomposition of ethanol and its intermediates occurs on active Pt sites, while dissociative adsorption of water happens over Sn sites to form oxygen-containing surface species. These oxygenated species react with poisonous intermediates, e.g., CO_{ads}, hence decreasing poisoning. According to the electronic effect, the presence of Sn modifies chemical properties of the Pt in such a way that the Pt–CO bonding is lowered. Furthermore, particle size also influences binding energy of CO_{ads} to Pt atoms. Carbon monoxide adsorbs much stronger on small Pt nanoparticles, which contain much greater proportion of "edge" sites, compared to the dominant proportion of "terrace" sites in larger nanoparticles [32, 36, 37]. The ratio of Pt atoms located on the "terrace" versus "edge" sites decreases with decreasing particle size [38]. Moreover, large Pt particles that weakly bond CO_{ads} are preferred over smaller particle. Therefore, the improved electrocatalytic activity of bi-phase Pt (6.5 nm)/SnO_x catalyst for ethanol electro-oxidation may be assigned to the bi-functional mechanism where one of the reaction steps includes interaction between weakly bonded CO_{ads} and oxygenated species provided by SnO_x phase.

4 Conclusions

Nanoparticulate Pt_7Sn_3 catalysts of controlled size were synthesized in ethylene glycol and further deposited on carbon support resulting in 20 wt% metal loading. Particle size was varied from 2.8 to 6.5 nm by adjusting the synthesis solution pH. We found that presence of sodium hydroxide in the synthesis solution influenced both the particle size and the resulting structure of nanoparticles. Disordered alloy Pt_7Sn_3 nanoparticles were formed at lower NaOH concentrations ($C_{NaOH} < 0.15$ M), while at the higher concentration ($C_{NaOH} \geq 0.15$ M), only partial alloying occurred and bi-phase Pt/SnO_x nanoparticles were found. Carbon supported Pt_7Sn_3 particles were tested for ethanol electro-oxidation. We found that bi-phase Pt (6.5 nm)/SnO_x showed the best catalytic activity for EOR among the prepared Pt_7Sn_3 samples followed by 5 nm disordered alloy Pt_7Sn_3 nano-catalyst. Disordered alloy and bi-phase Pt/SnO_x nanoparticles of 4.5–4.6 nm showed the same next best catalytic activity. Therefore, for the Pt_7Sn_3 catalysts prepared in the present work, performance towards EOR depended on the presence of nanoparticles with larger Pt surfaces and not on the

degree of alloying. This is attributed to the properties of ethanol which can adsorb only onto the sufficiently large Pt particles.

Acknowledgments Authors would like to thank Mr. Sander Mommers and Dr. Yun Liu from the Centre for Catalysis Research and Innovation (CCRI) for XPS and EDS/TEM measurements, respectively. This work was supported by Research Development Program at the University of Ottawa.

References

1. Song S, Tsiakaras P (2006) Appl Catal B: Environ 63:187
2. Tsiakaras P (2007) J Power Sour 171:102
3. Lamy C, Rousseau S, Belgsir EM, Coutanceau C, Leger J-M (2004) Electrochim Acta 49:3901
4. Jiang L, Sun G, Sun S, Liu J, Tang S, Li H, Zhou B, Xin Q (2005) Electrochim Acta 50:5384
5. Léger J-M, Rousseau S, Coutanceau C, Hahn F, Lamy C (2005) Electrochim Acta 50:5118
6. Zhou WJ, Song SQ, Li WZ, Zhou ZH, Sun GQ, Xin Q, Douvartzides S, Tsiakaras P (2005) J Power Sour 140:50
7. Jiang L, Colmenares L, Jusys Z, Sun GQ, Behm RJ (2007) Electrochim Acta 53:377
8. Bommersbach P, Chaker M, Mohamedi M, Guay D (2008) J Phys Chem C 112:14672
9. Garcia-Rodríguez S, Somodi F, Borbáth I, Margitfalvi JL, Pena MA, Fierro JLG, Rojas S (2009) Appl Catal B 91:83
10. Siné G, Foti G, Comninellis Ch (2006) J Electroanal Chem 595:115
11. Jiang L, Sun G, Zhou Z, Sun S, Wang Q, Yan S, Li H, Tian J, Guo J, Zhou B, Xin Q (2005) J Phys Chem B 109:8774
12. Zhu M, Sun G, Xin Q (2009) Electrochim Acta 54:1511
13. Zhou WJ, Song SQ, Li WZ, Sun GQ, Xin Q, Kontou S, Poulianitis K, Tsiakaras P (2004) Solid State Ion 175:797
14. Gupta SS, Singh S, Datta J (2009) Mater Chem Phys 116:223
15. Guo Y, Zheng Y, Huang M (2008) Electrochim Acta 53:3102
16. Alcala R, Shabaker JW, Huber GW, Sanchez-Castillo MA, Dumesic JA (2005) J Phys Chem B 109:2074
17. Li H, Sun G, Cao L, Jiang L, Xin Q (2007) Electrochim Acta 52:6622
18. Camara GC, de Lima RB, Iwasita T (2004) Electrochem Commun 6:812
19. Fujiwara N, Friedrich KA, Stimming U (1999) J Electroanal Chem 472:120
20. Ribeiro J, dos Anjos DM, Kokoh KB, Coutanceau C, Léger J-M, Olivi P, de Andrade AR, Tremiliosi-Filho G (2007) Electrochim Acta 52:6997
21. Debye P (1915) Ann Phys 46:809
22. Baranova EA, Le Page Y, Ilin D, Bock C, MacDougall B, Mercier PHJ (2009) J Alloys Compd 471:387
23. Harris IR, Norman M, Bryant AW (1968) J Less-Common Met 16:427
24. Le Page Y, Rodgers JR (2005) J Appl Crystallogr 38:697
25. Weissmann S (1981) Metal and alloys, data book vol 1. Center for diffraction data JCPDS, Pennsylvania
26. Baranova EA, Miles N, Mercier PHJ, Le Page Y, Patarachao B (2010) Electrochim Acta (in press). doi:10.1016/j.electacta.2009.12.090
27. Shukla AK, Arico AS, El-Khatib KM, Kim H, Antonucci PL, Antonucci V (1999) Appl Surf Sci 137:20
28. Hall SC, Subramanian V, Teeter G, Rambabu B (2004) Solid State Ion 175:809
29. Aricò AS, Antonucci V, Giordano N, Shukla AK, Ravikumar MK, Roy A, Barman SR, Sarma DD (1994) J Power Sour 50:295
30. Wagner CD, Riggs WM, Davis LE, Moulder JF, Muilenberg GE (1979) Handbook of X-ray photoelectron spectroscopy. Perkin-Elmer Corp, Eden Prairie
31. Eberhardt W, Fayet P, Cox DM, Fu Z, Kaldor A, Sherwood R, Sondericker D (1990) Phys Rev Lett 64:780
32. Baranova EA, Bock C, Ilin D, Wang D, MacDougall B, Wu X (2006) Surf Sci 600:3502
33. Bock C, Paquet C, Couillard M, Botton GA, MacDougall BR (2004) J Am Chem Soc 126:8028
34. Sheppard SA, Campbell SA, Smith JR, Lloyd GW, Ralph TR, Walsh FC (1998) Analyst 123:1923
35. Vigier F, Coutanceau C, Hahn F, Belgsir EM, Lamy C (2004) J Electroanal Chem 563:81
36. Park S, Wasileski SA, Weaver MJ (2001) J Phys Chem B 105:9719
37. Chang S-C, Weaver MJ (1991) J Phys Chem 95:5391
38. Nashner MS, Frenkel AI, Adler DL, Shapley JR, Nuzzo RG (1998) J Am Chem Soc 120:8093